Theoretical study of the electromigration wind force for adatom migration at metal surfaces

D. N. Bly and P. J. Rous
Department of Physics, University of Maryland Baltimore County, Baltimore, Maryland 21228
(Received 13 November 1995)

We present the results of a theoretical investigation of the electromigration wind force for adatom migration in a number of migrator-substrate systems. The theoretical background for our study follows from previous work done on bulk electromigration using the linear-response formalism of Kubo. We treat the electronic structure of the substrate using the layer Korringa-Kohn-Rostoker method, which allows us to examine, not only the general diffusion bias of the migrating ion, but also the variation of the wind force between adsorption sites. The interpretation of our findings in terms of a ballistic model of the wind force is discussed. [S0163-1829(96)00119-1]

I. INTRODUCTION

When an electrical current flows through a conducting solid, the migration of ions and point defects within the material can result.[1] This motion, known as electromigration, is manifest as a bias in the diffusion of defects and impurities through the material in a direction parallel, or antiparallel, to the applied electric field. Prior theoretical investigations of this phenomenon, in bulk materials, have exposed fundamental questions regarding the nature of the forces involved,[2–7] of particular interest being the screening of the direct interaction between the ion and the applied field. Nevertheless, experimental and theoretical studies of electromigration in bulk materials have lead to a general consensus concerning the dominant contribution to the driving force.[2]

Recent experimental studies have demonstrated that electromigration also occurs at the surfaces of solids and can have a profound influence upon the development of surface morphology in the presence of an electric field.[8–11] The theory of the driving force in surface electromigration has, however, received comparatively little attention with, to our knowledge, just four studies done to date.[12–15] In this paper, we present a theoretical and computational study of the wind force in electromigration at the surfaces of metals. This investigation utilizes a layer Korringa-Kohn-Rostoker (LKKR) method to compute the electron-scattering states and thereby the driving force, due to electronic conduction, experienced by an isolated adatom at a surface. Preliminary results of this work have been presented elsewhere.[15]

From the earliest stages in the development of bulk electromigration theory, the force acting upon the migrating ion has been separated into two components to which effective valences can be assigned,[16,17]

$$\mathbf{F}=e\mathbf{E}(Z_d+Z_w). \tag{1}$$

The first term on the right-hand side of this equation represents the force acting on the ion through its ''direct'' interaction, with the external applied field **E**. This component of the net driving force is usually referred to as the *direct force*. The other contribution to the driving force, *the wind force*, is associated with the momentum exchange between the current carriers and the migrator.

For bulk electromigration in a free-electron metal, the magnitude of the wind valence, Z_w, can be estimated from a ballistic model:[16,17] $Z_w=-n_0 l\sigma_{\rm tr}$, where n_0 is the electron concentration, l is the electronic mean free path, and $\sigma_{\rm tr}$ is the transport cross section of the adatom evaluated at the Fermi energy. For a typical metal [$n_0\sim10^{-1}$ Å^{-3}, $l\sim100$ Å and $\sigma_{\rm tr}\sim1$ Å^2 (Ref. 18)], the ballistic model predicts that $Z_w\sim-10$, a result which suggests that the wind force dominates the direct component of the driving force $|Z_d|\sim1$. Although multiple scattering of the conduction electrons between the migrator and the host modify this simple picture, the wind force is generally the dominant force in bulk electromigration and consequently there has been considerable theoretical effort expended in the quantitative calculation of Z_w for many migrator-host systems.[3,17,19–24]

In this work, we present a quantitative calculation of the wind force experienced by an isolated adatom at the surface of a metal in the presence of a time independent applied electric field. The organization of this paper is as follows: In Sec. II, we review the basic theory of the driving force in electromigration, which is based upon the linear-response formalism of Kubo and was developed originally for bulk electromigration by Kumar and Sorbello,[12] Lodder and co-workers,[20,25] and Gupta.[21] In particular, we show that the force can be expressed in terms of the single-particle states of the substrate the representation and computation of which, by a layer-KKR method, is described in Sec. III and IV. Section V covers some further aspects of the computation and Sec. VI details the application of this theory to several different migrator-substrate systems. The results are compared to previous work[13] and to the ballistic model of electromigration at surfaces.

II. THEORETICAL BACKGROUND: LINEAR-RESPONSE THEORY

We seek an expression for the force experienced by an isolated adatom located on a metallic surface in the presence of a constant applied electric field **E**. Following Kumar and Sorbello,[12] the force on a single adatom is defined as the rate of change of the expectation value of its momentum **P**,[26]

$$\frac{d\langle \mathbf{P}\rangle}{dt} = -i\langle[\mathbf{P},\mathscr{H}]\rangle, \tag{2}$$

where $\mathscr{H}$ is the Hamiltonian of the adatom-surface system in an applied electric field $\mathbf{E}(t)$. We write $\mathscr{H}$, assuming a separation of the substrate charge density into localized and itinerant parts, as

$$\mathscr{H} = \mathscr{H}_e + \mathscr{H}_a + \mathscr{V}^{\cdot} + e\left(\sum_m \mathbf{r}_m - Z\mathbf{R}\right)\cdot\mathbf{E}(t). \tag{3}$$

The first two terms,

$$\mathscr{H}_e = \mathscr{T}_e + \mathscr{V}_e^s \tag{4}$$

and

$$\mathscr{H}_a = \mathscr{T}_a + \mathscr{V}_a^s, \tag{5}$$

include the interactions of the adatom, $\mathscr{V}_a^s$, and substrate conduction electrons, $\mathscr{V}_e^s$, with the static charge associated with the substrate ion cores. $\mathscr{V}^{\cdot}$ is the interaction potential between the adatom and the conduction electrons of the metallic substrate. The last two terms on the right-hand side of Eq. (3) represent the interaction of the migrating adatom and the conduction electrons with the electric field. The sum is over the coordinates of the conduction electrons and $\mathbf{R}$ is the position vector of the adatom, of valence Z.

Substituting for $\mathscr{H}$ [Eq. (3)] in Eq. (2), we obtain the total force experienced by the adatom,

$$\frac{d\langle \mathbf{P}\rangle}{dt} = Ze\mathbf{E}(t) - \langle \nabla_{\mathbf{R}}\mathscr{V}_a^s\rangle - \langle \nabla_{\mathbf{R}}\mathscr{V}^{\cdot}\rangle. \tag{6}$$

In this expression, the first term on the right may be identified as the force, due to the ''direct'' interaction of the adatom with the applied field, the second term describes the force on the migrating adatom, due to interaction with the substrate ion cores. The third term is the component of the driving force generated by the interaction of the adatom with the conduction-electron charge density.

To evaluate the term, $\langle \nabla_{\mathbf{R}}\mathscr{V}^{\cdot}\rangle$, appeal is made to the linear-response formalism of Kubo.[27] The equation of motion of a state operator $\rho(t)$ in the presence of a time-dependent perturbation $\mathscr{H}'(t)$ is

$$i\,\frac{\partial\rho(t)}{\partial t} = [\mathscr{H}_0 + \mathscr{H}'(t), \rho(t)] - \frac{i[\rho(t)-\rho_0]}{\tau}, \tag{7}$$

where we have introduced a time constant, τ, that sets the time scale of relaxation of the electronic charge density. The perturbed state operator is written as

$$\rho(t) = \rho_0 + \Delta\rho(t), \tag{8}$$

where $\lim_{t\to-\infty}\rho(t) = \rho_0$ is the state operator in the absence of the perturbation $\mathscr{H}'(t)$. Solving this equation and retaining only terms linear in the perturbation gives

$$\Delta\rho(t) = -i\int_{-\infty}^{t} e^{i\mathscr{H}_0(t'-t)} \times [\mathscr{H}'(t'), \rho_0]e^{-i\mathscr{H}_0(t'-t)}e^{[(t'-t)/\tau]}dt'. \tag{9}$$

Thus, the expectation value of an observable $\mathscr{A}$ is

$$\langle \mathscr{A}\rangle(t) = \mathrm{Tr}[\rho_0\mathscr{A}] + \mathrm{Tr}[\Delta\rho(t)\mathscr{A}]. \tag{10}$$

In the spirit of the Born-Oppenheimer approximation, we assume that time scales of the variations in the total state operator, due to the perturbation of the electronic configuration under the applied field and due to the motion of the ion are disparate. This allows us to treat the position of the adatom, $\mathbf{R}$, as a fixed parameter and perform the calculation in a basis of electronic states. We note that, in this approximation, the term $\langle \nabla_{\mathbf{R}}\mathscr{V}_a^s\rangle$ in Eq. (6) contributes a constant to $\partial\rho(t)/\partial t$ for a given $\mathbf{R}$. Defining $\mathscr{A} = \nabla_{\mathbf{R}}\mathscr{V}^{\cdot}$ and $\mathscr{H}'(t) = e\mathbf{E}(t)\cdot\Sigma_m\mathbf{r}_m$ and substituting into Eq. (10), we obtain directly

$$\langle \nabla_{\mathbf{R}}\mathscr{V}^{\cdot}\rangle = \mathrm{Tr}[\rho_0\nabla_{\mathbf{R}}\mathscr{V}^{\cdot}] - i\int_{-\infty}^{t}\mathrm{Tr}\{e^{i\mathscr{H}_0(t'-t)} \times [e\mathbf{E}(t')\cdot\Sigma_m\mathbf{r}_m, \rho_0]e^{-i\mathscr{H}_0(t'-t)}\nabla_{\mathbf{R}}\mathscr{V}^{\cdot}\} \times e^{[(t'-t)/\tau]}dt', \tag{11}$$

where the traces are over many-body states of the electronic system. As ρ_0 represents a state with no net electron flux, the second term on the right contains all contributions to the force, due to charge motion, and therefore, can be identified as the wind force experienced by the adatom. To proceed further we assume that the Hamiltonian of the electronic system may be written as a sum over a single-particle Hamiltonians, allowing us to write the trace over single electron states:

$$\mathbf{F}_{\mathbf{w}} = ie\int_{-\infty}^{t} dt'\ \mathrm{tr}[[\mathbf{E}(t')\cdot\mathbf{r}, \mathbf{f}_0]e^{-i\Gamma(t'-t)}\nabla_{\mathbf{R}}v]e^{[(t'-t)/\tau]}, \tag{12}$$

with

$$\mathbf{f}_0 = [e^{\beta(\mathbf{h}-E_F)}+1]^{-1}. \tag{13}$$

$\mathbf{\Gamma}$ is a Liouville operator with the property $\mathbf{\Gamma\Omega} = [\mathbf{h},\mathbf{\Omega}]$ and v is the interaction energy of a single electron with the migrator. Taking the time dependence of the applied electric field to be $\mathbf{E}(t) = \mathbf{E}\cos(\omega t)$ the integral over time may then be performed to give limit $\omega\to 0$,

$$\mathbf{F}_w = ie\ \mathrm{tr}\left[\left(\frac{1}{i\mathbf{\Gamma}+\tau^{-1}}\right)[\mathbf{E}\cdot\mathbf{r}, \mathbf{f}_0]\nabla_{\mathbf{R}}v\right]. \tag{14}$$

By expanding the $\mathbf{f}_0$ operator and employing the identity

$$[\mathbf{\Omega}, e^{-\beta\mathbf{h}}] = e^{-\beta\mathbf{h}}\int_0^{\beta} e^{\lambda\mathbf{h}}[\mathbf{h},\mathbf{\Omega}]e^{-\lambda\mathbf{h}}d\lambda, \tag{15}$$

Eq. (14) may be written as

$$\mathbf{F}_w = ie\ \mathrm{tr}\left[\left(\frac{1}{i\mathbf{\Gamma}+\tau^{-1}}\right)(1-\mathbf{f}_0)\int_0^{\beta} d\lambda(-i)\mathbf{E}\cdot\dot{\mathbf{r}}(-i\lambda)\mathbf{f}_0\nabla_{\mathbf{R}}v\right], \tag{16}$$

where $\dot{\mathbf{r}}$ is the electron velocity operator. Taking the trace in eigenstates of $\mathbf{h}$ yields the usual working expression for the wind force,[25]

$$\mathbf{F}_w(\mathbf{R}) = -\sum_{\mathbf{k}} g(\mathbf{k}) \langle \psi_{\mathbf{k}} | \nabla_{\mathbf{R}} v(|\mathbf{R}-\mathbf{r}|) | \psi_{\mathbf{k}} \rangle, \tag{17}$$

with

$$g(\mathbf{k}) = e\tau(\mathscr{E}(\mathbf{k}))\dot{\mathbf{r}}(\mathbf{k})\cdot\mathbf{E}\,\frac{\partial f_0}{\partial \mathscr{E}_k}, \tag{18}$$

where we have assumed that the electronic relaxation time is purely energy dependent and have neglected higher-order distortions of the Fermi surface through terms in powers of $(-i\tau\mathbf{\Gamma})$ in the trace. In the low temperature limit, $\partial f_0/\partial \mathscr{E}_k \rightarrow -\delta(\mathscr{E}-\mathscr{E}_F)$ and we may rewrite Eq. (17) in the form

$$\mathbf{F}_w(\mathbf{R}) = \frac{e\Omega}{4\pi^3}\int\int_{\mathrm{FS}} \frac{\mathbf{d}^2\mathbf{k}}{|\nabla \mathscr{E}_k|}\,\tau_{\mathscr{E}}\mathbf{v}_F(\mathbf{k})\cdot\mathbf{E}\int\int\int \mathbf{d}^3\mathbf{r}\,\psi^*_{\mathbf{k}}(\mathbf{r})\nabla_{\mathbf{R}} v(|\mathbf{R}-\mathbf{r}|)\,\psi_{\mathbf{k}}(\mathbf{r}), \tag{19}$$

where the electron states are normalized to Ω, the volume of a substrate unit cell.

For the surface electromigration of an adatom, the wind force will, in general, be anisotropic and dependent upon the location of the adatom within the surface unit cell. Therefore, we represent the wind force, given by Eq. (19), by an effective valence tensor $\underline{Z}_w$, defined such that

$$\mathbf{F}_w(\mathbf{R}) = e\underline{Z}_w(\mathbf{R})\mathbf{E}. \tag{20}$$

Comparing Eqs. (19) and (20), the components of the (Cartesian) effective valence tensor are defined as

$$(Z_w)_{ij} = \int\int_{\mathrm{FS}} \frac{\mathbf{d}^2\mathbf{k}}{|\nabla_{\mathbf{k}}\mathscr{E}_{\mathbf{k}}|}\,\tau_{\mathscr{E}}[\mathbf{v}_F(\mathbf{k})\cdot\hat{\mathbf{x}}_j]I_i(\mathbf{k},\mathbf{R}), \quad i,j=x,y, \tag{21}$$

where

$$I_i(\mathbf{k},\mathbf{R}) = \frac{\Omega}{4\pi^3}\int\int\int \psi^*_{\mathbf{k}}(\mathbf{r})\psi_{\mathbf{k}}(\mathbf{r})[\nabla_{\mathbf{R}} v(|\mathbf{R}-\mathbf{r}|)\cdot\hat{\mathbf{x}}_i]\mathbf{d}^3\mathbf{r}. \tag{22}$$

Evaluation of the wind force experienced by an adatom requires the evaluation of the one-electron scattering states of the substrate, $\psi_{\mathbf{k}}$. Our approach, utilizing a LKKR calculation, is described in the following sections.

III. REPRESENTATION OF THE ELECTRON-SCATTERING STATES

To evaluate the conduction electron states in the vicinity of the adatom, we adopt the muffin-tin approximation and confine the atomic potentials to nonoverlapping spheres with a constant interstitial potential. The scattering properties of each atom are characterized by a set of phase shifts, which we denote by δ_l for substrate atoms and by δ_l^a for the adatom. This allows us to expand the electron states in a partial wave basis,

$$\psi_{\mathbf{k}}(\mathbf{r}) = \frac{4\pi}{\sqrt{\Omega}}\sum_{lm} i^l A_{lm}(\mathbf{k}) R_l(r) Y_{lm}(\hat{\mathbf{r}}), \tag{23}$$

where R_l is the radial solution of the Schrödinger equation. In the interstitial region surrounding the adatom, the electronic wave functions are spherical waves, so that Eq. (23) becomes

$$\psi_{\mathbf{k}}(\mathbf{r}) = \frac{4\pi}{\sqrt{\Omega}}\sum_{lm} i^l A_{lm}(\mathbf{k})[j_l(\kappa r) + h_l^{(1)}(\kappa r) \times i e^{i\delta_l^a}\sin\delta_l^a] Y_{lm}(\hat{\mathbf{r}}), \tag{24}$$

where $\kappa = \sqrt{2\mathscr{E}_{\mathbf{k}}}$, j_l is a spherical Bessel function, $h_l^{(1)}$ is a spherical Hankel function of the first kind, and Y_{lm} is a spherical harmonic. The coefficients of the spherical wave expansion, A_{lm}, are obtained from the layer-KKR calculation described in Sec. IV.

Having obtained the expansion of ψ_k in spherical waves, we substitute into Eq. (22) giving, with the adatom located at the origin of coordinates,

$$I_j(\mathbf{k}) = \frac{4}{\pi}\sum_{lm}\sum_{l'm'} i^{l'-l} A^*_{lm}A_{l'm'} \times \int dr\; r^2 R^*_l(r) R_{l'}(r)\,\frac{dV(r)}{dr} \times \int\int \mathbf{d}^2\hat{r}\, Y^*_{lm}(\hat{\mathbf{r}})Y_{l'm'}(\hat{\mathbf{r}})(\hat{\mathbf{r}}\cdot\hat{\mathbf{x}}_j). \tag{25}$$

The angular integral is

$$\int Y^*_{lm}(\hat{\mathbf{r}})Y_{l'm'}(\hat{\mathbf{r}})(\hat{\mathbf{r}}\cdot\hat{\mathbf{x}})\mathbf{d}^2\hat{\mathbf{r}} = \int\int Y^*_{lm}(\hat{\mathbf{r}})Y_{l'm'}(\hat{\mathbf{r}})\sin^2\theta\,\cos\phi\; d\theta\; d\phi = (-1)^m\sqrt{2\pi/3}(C_{l,-m;l',m';1,-1} - C_{l,-m;l',m';1,+1}) \tag{26}$$

and

$$\int Y^*_{lm}(\hat{\mathbf{r}})Y_{l'm'}(\hat{\mathbf{r}})(\hat{\mathbf{r}}\cdot\hat{\mathbf{y}})\mathbf{d}^2\hat{\mathbf{r}} = \int\int Y^*_{lm}(\hat{\mathbf{r}})Y_{l'm'}(\hat{\mathbf{r}})\sin^2\theta\,\sin\phi\; d\theta\; d\phi = (-1)^m i\sqrt{2\pi/3}(C_{l,-m;l',m';1,-1} + C_{l,-m;l',m';1,+1}), \tag{27}$$

where C is a Clebsch-Gordan coefficient.

The radial integral of Eq. (25) is a standard result from the theory of the electron-phonon interaction,[28,29]

$$\int r^2 R_l^*(r) R_{l'}(r) \frac{dV(r)}{dr} dr = \pm 4 e^{i(\delta_{l'}^a - \delta_l^a)} \sin(\delta_l^a - \delta_{l'}^a), \quad l' = l \pm 1. \tag{28}$$

Combining these results [Eqs. (29) and (25)], we find our final expression for $I(\mathbf{k})$ in terms of the spherical wave expansion coefficients, A_{lm} of the electron scattering states:

$$I_j(\mathbf{k}) = \sum_{lm} \sum_{l'=l\pm1} \sum_{m'=m\pm1} (-1)^m A_{lm}^* A_{l'm'} \times \sin^2(\delta_l^a - \delta_{l'}^a) B_j(lm, l'm'), \quad j = x, y, \tag{29}$$

where

$$B_x(lm, l'm') = (C_{l,-m;l',m';1,-1} - C_{l,-m;l',m';1,1}),$$

$$B_y(lm, l'm') = \imath (C_{l,-m;l',m';1,-1} + C_{l,-m;l',m';1,1}).$$

Thus, to calculate the wind force from Eq. (29), the spherical-wave expansion coefficients, A_{lm} of the conduction electronic states must be evaluated. This part of the calculation is performed by the layer-KKR method described in the next section.

IV. LAYER-KKR CALCULATION

The LKKR method constructs the scattering properties of the substrate by assembling single atoms into atomic planes, which are then combined into a semi-infinite stack representing the bulk termination of the solid. The theoretical basis of the method has been described in detail elsewhere.[30,31] Here, we review the basic computational procedures relevant to the computation of the wind force experienced by an adatom on a current carrying substrate.

The procedure is to partition a model surface potential, calculate the substrate scattering properties and then embed the molecule into the surface barrier; each stage requiring the solution of a multiple-scattering problem for which we use standard computational techniques from the theory of low-energy electron diffraction.[32] For computational convenience, the surface potential is separated into three regions by two planes oriented parallel to the surface. The first, P_S, is positioned a distance of one half of the bulk interplanar spacing above the top layer of substrate atoms; the second, P_M, passes through the center of mass of the molecule. Region *III* contains the crystalline substrate consisting of a stack of atomic planes, regions *I* and *II* contain the surface barrier (see Fig. 1). At each plane, the electronic states may be expressed as a linear combination of the substrate Bloch states,

$$\psi(\mathbf{r}) = \sum_{\mathbf{k}_\parallel} \sum_{\mathbf{g}} A_{\mathbf{g}}^+(\mathbf{k}_\parallel) e^{i(\mathbf{k}_\parallel + \mathbf{g})\cdot\mathbf{r}_\parallel} e^{iK_{\mathbf{g}z}^+ z} + A_{\mathbf{g}}^-(\mathbf{k}_\parallel) e^{i(\mathbf{k}_\parallel + \mathbf{g})\cdot\mathbf{r}_\parallel} e^{iK_{\mathbf{g}z}^- z}, \tag{30}$$

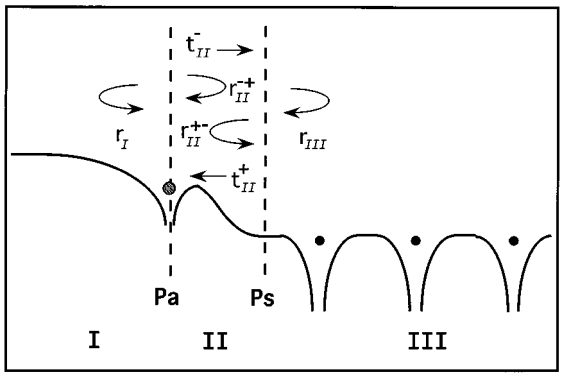

FIG. 1. Schematic representation of the adatom-surface system illustrating the operator notation used in the text. P_A and P_S are planes lying parallel to the surface located at the adatom and one-half layer spacing above the surface, respectively. The *r* and *t* denote the reflection and transmission operators of the substrate and surface barrier.

where $\mathbf{k}_\parallel$ is the component of momentum parallel to the surface, $\mathbf{g}$ is a reciprocal-lattice vector of the substrate, the electron wave vector is

$$\mathbf{K}_{\mathbf{g}}^{\pm} = (\mathbf{k}_\parallel + \mathbf{g}, \pm K_{\mathbf{g}z}), \tag{31}$$

where $K_{\mathbf{g}z}$ is the component of momentum perpendicular to the substrate,

$$K_{\mathbf{g}z} = \sqrt{2E - |\mathbf{k}_\parallel + \mathbf{g}|^2}. \tag{32}$$

The substrate scattering may be evaluated efficiently by first determining the $\mathbf{k}_\parallel$-resolved reflection coefficients of the substrate, $r_{\mathbf{gg}'}^{III}(\mathbf{k}_\parallel)$. The substrate is represented as a stack of atomic planes parallel to the surface. After determining the atomic phase shifts, the scattering paths within one atomic layer parallel to the surface are summed, using the Kambe method.[33–35] The atomic planes are then assembled into the semi-infinite termination of the crystal surface, using the layer doubling algorithm[30] to sum the interlayer multiple-scattering paths. The $\mathbf{k}_\parallel$-resolved reflection and transmission coefficients of the barrier regions, $r_{\mathbf{gg}'}^{I}(\mathbf{k}_\parallel)$, $t_{\mathbf{gg}'}^{II+}(\mathbf{k}_\parallel)$, $r_{\mathbf{gg}'}^{II+-}(\mathbf{k}_\parallel)$, $r_{\mathbf{gg}'}^{II-+}(\mathbf{k}_\parallel)$, and $t_{\mathbf{gg}'}^{II-}(\mathbf{k}_\parallel)$ are evaluated, for a given position, z_a, of the adatom relative to the upper atomic plane of the substrate, by numerical integration of the Schrödinger equation.

Given these quantities, the *k*-resolved reflection coefficients, of the right and left half spaces, $\mathscr{R}_R(\mathbf{k})$ and $\mathscr{R}_L(\mathbf{k})$ relative to the plane containing the molecule (P_M) may be obtained by summing the multiple-scattering series by matrix inversion,

$$\mathscr{R}_L = r_I, \tag{33}$$

$$\mathscr{R}_R = r_{II}^{-+} + t_{II}^- r_{III} (1 - r_{II}^{+-} r_{III})^{-1} t_{II}^+. \tag{34}$$

The surface scattering operator, for a given $\mathbf{k}_\parallel$, is found by summing over all scattering paths originating and ending on the adatom:

$$\tau_{lm,l'm'}(\mathbf{k}_\parallel,E)=\sum_{\mathbf{g}}\sum_{\mathbf{g}'}\tilde{\Lambda}^{\pm}_{lm,\mathbf{g}}(\mathbf{k}_\parallel)\,\tau_{\mathbf{g}\mathbf{g}'}\Lambda^{\pm}_{\mathbf{g}',l'm'}(\mathbf{k}_\parallel), \tag{35}$$

$$\tau_{\mathbf{g}\mathbf{g}'}(\mathbf{k}_\parallel,E)=[(1-\mathscr{R}_R\mathscr{R}_L)^{-1}(\mathscr{R}_R+\mathscr{R}_R\mathscr{R}_L) +\mathscr{R}_L(1-\mathscr{R}_R\mathscr{R}_L)^{-1}(1+\mathscr{R}_R)]_{\mathbf{g}\mathbf{g}'}, \tag{36}$$

where the operator Λ projects outgoing spherical waves into a plane-wave basis,

$$\Lambda^{\pm}_{lm,\mathbf{g}}(\mathbf{k}_\parallel)=\frac{2\pi i}{\Omega\kappa|K_{\mathbf{g}z}|}\,Y_{lm}(\hat{\mathbf{K}}^{\pm}_g), \tag{37}$$

and the inverse operator $\tilde{\Lambda}$ projects plane waves into an angular momentum basis.[36]

$$\tilde{\Lambda}^{\pm}_{\mathbf{g},lm}(\mathbf{k}_\parallel)=4\pi i^l Y^*_{lm}(\hat{\mathbf{K}}^{\pm}_g). \tag{38}$$

The full scattering matrix of the surface is then obtained by integration of τ over the two-dimensional Brillouin zone (area Ω) containing $\mathbf{k}_\parallel$

$$\mathscr{S}_{lm,l'm'}(E)=\frac{1}{\Omega}\int\int_{\Omega}\tau_{lm,l'm'}(\mathbf{k}_\parallel,E)\,\mathbf{d}^2\mathbf{k}_\parallel. \tag{39}$$

Multiple scattering between the plane containing the adatom and the substrate is described in an angular momentum basis, where the substrate scattering is defined by the surface scattering operator, $\mathscr{S}$, describing the reflection of an outgoing spherical wave by the surface into a set of incoming waves outside of the muffin-tin sphere centered on the adatom,

$$h^{(1)}_l(\kappa r)Y_{lm}(\hat{\mathbf{r}})\rightarrow h^{(1)}_l(\kappa r)Y_{lm}(\hat{\mathbf{r}}) +\sum_{l'm'}\mathscr{S}_{l'm',lm}j_{l'}(\kappa r)Y_{l'm'}(\hat{\mathbf{r}}). \tag{40}$$

If the conduction electronic states in the absence of the adatom are expanded about the origin as

$$\psi^0_{\mathbf{k}}(\mathbf{r})=\frac{4\pi}{\sqrt{\Omega}}\sum_{lm}i^l A^0_{lm}(\mathbf{k})j_l(\kappa r)Y_{lm}(\hat{\mathbf{r}}), \tag{41}$$

the introduction of the adatom modifies the spherical wave coefficients as follows:

$$A_{lm}(\mathbf{k})=(1-t_a\mathscr{S})^{-1}A^0_{lm}(\mathbf{k}), \tag{42}$$

where t_a is the operator describing scattering by the adatom. The principal modification of the standard LKKR calculation is the evaluation the surface scattering matrix $\mathscr{S}$, using multiple-scattering theory. The computation of the conduction electron states of the substrate, and more specifically, their expansion coefficients A^0_{lm} are achieved by a straightforward modification of the standard LKKR method and, consequently, will not be discussed in detail here.

V. COMPUTATIONAL DETAILS

For the substrates considered in this paper, the surface-barrier potential was obtained from the saturated image potential model of Jennings, Jones, and Jepsen,[37] with parameters fitted to the binding energy of image states,[38]

$$V_b(z)=\frac{e^{-\lambda(z-z_0)}-1}{2(z-z_0)},\quad z>z_0, \tag{43}$$

$$\frac{-U_0}{Ae^{\beta(z-z_0)}+1},\quad z<z_0. \tag{44}$$

The presence of the adatom locally distorts the surface barrier and such a distortion could be modeled by performing a Fourier expansion of the barrier potential and then separately numerically integrating each Fourier component of the electron wavefield through the barrier. However, in the case of an isolated adatom, such a procedure requires a large number of Fourier components to obtain a convergent description of scattering by the (distorted) surface barrier, in addition to the introduction a large number of free parameters into the description of the surface barrier. To limit the number of such parameters introduced into the calculation, the surface barrier was assumed to be uncorrugated and fixed, such that the origin ($z=0$) of the barrier potential was located one half of a bulk interlayer substrate spacing beyond the adatom.

In the treatment of atomic scattering [see, for example, Eq. (29)], we employed partial wave contributions up to $l_{\max}=3$. In order to evaluate the surface scattering matrix, it is necessary to add a small imaginary part V_{0i} to the interstitial potential. This imaginary part of the potential serves to damp the electron wavefield in the surface and ensures convergence of the layer doubling algorithm. In the calculations reported in this paper, $0.02\leqslant V_{0i}=\leqslant 0.04Ha$. The integral over the surface Brillouin zone [Eq. (39)] was performed using the method of special points;[39] we include 134 quadrature nodes within the irreducible wedge of the zone.

VI. RESULTS

Introduction

Utilizing the LKKR method described above, we have calculated the wind force acting upon isolated adatoms along typical migration pathways that link high-symmetry surface binding sites. We have determined the averaged effective valence for migration between these sites and computed the variation of the wind force, as a function of the adatom height and lateral position. Using these results, we have examined the validity of a ballistic interpretation of the wind force for the surface electromigration of adatoms.

In Sec. VI A 1, we present the results of a LKKR calculation for adatom self-electromigration on Na(100). Our findings are compared with those of a prior theoretical investigation by Duryea and Huntington, who employed the jellium model to determine the wind force for surface electromigration on Na(100).[13] In Sec. VI A 2, we consider the self-electromigration of isolated adatoms on the low Miller index faces of copper; Cu(110), Cu(100), and Cu(311). The self-electromigration of adatoms on Cu(111) was the subject of a prior publication.[15] Finally, in Sec. VI A 3, we present the results of a study of impurity electromigration on a copper substrate.

For each system investigated, it was assumed that the substrate consisted of an unreconstructed cleavage of the bulk

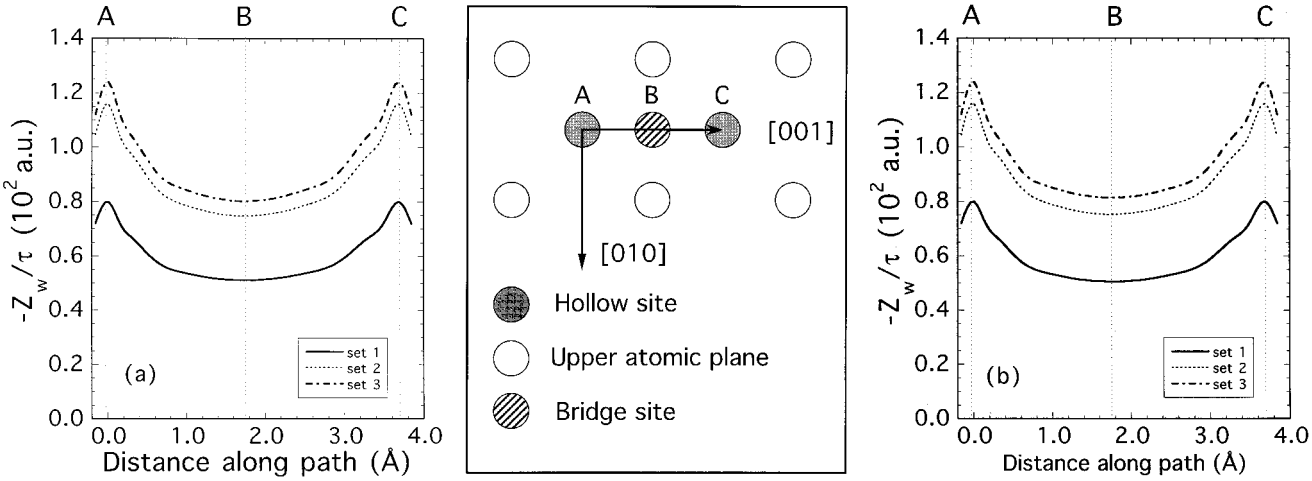

FIG. 2. Calculated effective wind valence for adatom self-electromigration on Na(100), shown as a function of the distance along the migration pathway (see schematic), parallel to the [010] direction and linking two hollow sites (*A* and *C*) via a bridge site (*B*). Z_w is normalized to the bulk relaxation time τ. The component of Z_w/τ coupling the applied **E** to the wind force in the same direction is given. (a) The applied field is in the [010] direction. (b) The applied field is in the [001] direction. The calculated effective valence is shown for three sets of adatom phase shifts employed by Duryea and Huntington (Ref. 13): set 1 (solid curve), set 2 (dashed curve), and set 3 (dot-dashed curve) (see text).

lattice. The Cartesian components of the wind force were calculated as the isolated adatom was stepped along predefined migration paths. The migration paths were chosen to lie between continuation sites of the crystal surface and represent plausible diffusion routes. As an adatom moves along a migration path, the height of the adatom above the substrate changes. In order to approximately model this variation, at each discrete point on a migration pathway for which the driving force was computed, the adatom height was adjusted so that the nearest-neighbor distance was the mean of the metallic radii of the adatom and substrate atom. For Cu(111), this simple procedure yielded adsorption heights that were not significantly different (± 0.1 Å) from those obtained from an embedded-atom method calculation of local geometry of the adatom.[15]

In order to generate the Cartesian components of the wind valence tensor, Z_w, calculations were performed for an external electric field applied in two orthogonal directions in a plane parallel to the substrate. The calculated wind force was expressed as an effective valence, Z_w, normalized to the relaxation time τ. As temperature dependence enters the problem primarily through the substrate resistivity, this representation has the virtue of being temperature independent. The quoted absolute values of Z_w employed published *bulk* values of τ. Clearly, if the relaxation time at the surface differs significantly from the bulk value then this procedure provides only an estimate of the absolute valence and Z_w/τ offers a more appropriate, quantitative, measure of the driving force.

1. Self-electromigration on Na(100)

Using the ballistic, momentum-transfer, theory of Huntington and Grone[17] and Fiks,[16] Duryea and Huntington[13] computed the wind force for a sodium atom interacting with a jellium model of a sodium substrate. These prior results predict that the effective valence of a Na migrator in bulk jellium is $-8.6 \geqslant Z_w \geqslant -13.8$ at 85 °C. As the adatom passed through the jellium edge, into the vacuum region, the magnitude of the wind force increased beyond its bulk value and exhibited a maximum, where Z_w increased by a factor of approximately three over its bulk value. As would be expected for a jellium calculation, the wind force was strictly antiparallel to the direction of electron flow.

In Fig. 2, we display the effective valence, determined by a LKKR calculation, of the wind force for adatom self-electromigration on Na(100). The migration pathway considered lies parallel to the [010] direction and links two fourfold hollow sites *via* the twofold bridge site (see schematic accompanying Fig. 2). In order to compare our results with those of the prior jellium model, the wind force was computed for the same three sets of Na adatom scattering phase shifts employed by Duryea and Huntington.[40] For each adatom position along the migration pathway, the components of the driving force parallel and perpendicular to the applied field were computed. These two components of the force, computed separately for electric fields parallel to the [010] and [001] directions, yield the elements of the Cartesian valence tensor.

Figure 2 displays the variation of the diagonal elements of the effective valence tensor coupling applied fields and wind forces in the [010] [Fig. 2(a)] and [001] [Fig. 2(b)] directions. In essence, these are the components of the driving force parallel to the electric field when the field is applied parallel to either the [010] or [001] directions. The off-diagonal elements of the effective valence tensor, which describe the components of the driving force perpendicular to the applied field, were found to be approximately two orders of magnitude smaller than the diagonal elements.[41] This result indicates that, to a very good approximation, the wind force for self-electromigration on Na(100) is antiparallel to the applied field, for any adatom location on the migration pathway considered. Further, since the magnitudes of the diagonal elements of Z_w shown in Fig. 2 are almost identical, the calculated wind force is found to be highly isotropic.

These features would be expected from a simple ballistic model of the driving force where the direction of the wind force would be strictly antiparallel to the field and the magnitude of the wind force would be independent of the direction of the **E**. This result suggests that the wind force for self-electromigration on Na(100) is highly ballistic in nature, as would be anticipated for a simple metal such as sodium.

Although the magnitude of the wind force is dependent upon the location of the adatom on the migration pathway, its variation is qualitatively similar for each of the three sets of adatom phase shifts. In agreement with Duryea and Huntington,[13] we find that the choice of adatom phase shifts significantly affects the calculated magnitude of the force. Using published values for the bulk resistivity of sodium,[42] we estimated the electronic relaxation time to be $\tau \approx 1495$ a.u. and computed the average wind valence between the fourfold symmetric hollow sites *via* the proposed migration path. We note that since the electromigration the wind force serves to bias a thermally activated diffusion process, the relevant valence is that averaged along the segment of the path between the initial binding site (hollow site) and the saddle point (bridge site). Using this procedure, averaged effective valence of the adatom was found to be $-8.4 \geqslant \langle Z_w \rangle \geqslant -13.6$ at 295 K, independent of the direction of the applied field. The range of values arises, because three different sets of phase shifts were employed in the calculation. The calculated value of effective valence for surface self-electromigration in Na(100) obtained by the LKKR method agrees well with the *bulk* valence determined by from the jellium calculation performed by Duryea and Huntington [$-8.6 \geqslant Z_w \geqslant -13.8$ at 85 °C (Ref. 13)].

In order to show how the wind force depends upon the adatom height, in Fig. 3, we display the calculated variation of the Z_w/τ as a function of the height of the adatom above the first atomic plane of the substrate. The applied field is parallel to the [010] direction and Z_w/τ calculated when the adatom was located above the hollow and the bridge sites of Na(100) are shown. From Fig. 3, we observe that the magnitude of the wind force passes through a maximum (for an adatom-surface separation of ≈ 1.5 Å), before decreasing rapidly as the adatom is moved away from the substrate. It is also interesting to note that the magnitude of driving force becomes independent of the adsorption site as the adatom is moved further than ≈ 2.5 Å from the substrate. For adsorption heights lower than 2.5 Å, the force at the bridge site was found to be slightly larger than at the hollow site.

These observations are consistent with a simple ballistic description of the wind force, where Z_w is directly proportional to the local density of conduction electrons at the adatom, $n(\mathbf{r})$, a quantity that rapidly decreases outside the substrate. The observed convergence of the wind forces for distinct adsorption sites, as the adatom moves away from the surface, is then a manifestation of the ''smoothing out'' of the lateral corrugation in $n(\mathbf{r})$ far from the surface. Careful comparison of Figs. 2 and 3 then leads us to the conclusion that the lateral variation of the wind force seen in Fig. 2 is a consequence of the variation of the adsorption height of the adatom (2.1 Å at the hollow site and 3.0 Å at the bridge site), and, therefore, the local density of conduction-electron states, as the Na atom is moved along the migration path. Thus, for the case of self-electromigration on Na(100), the wind force is found to be ballistic in origin and multiple scattering of conduction electrons between the adatom and host (substrate) is of little importance in determining the driving force.

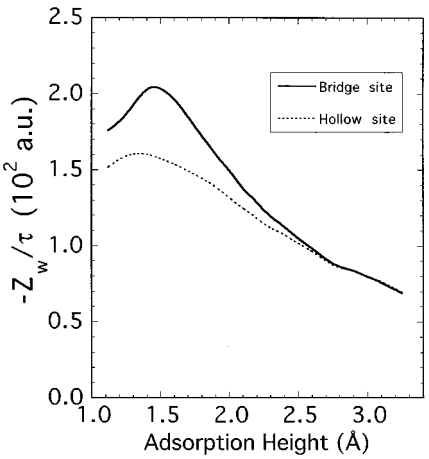

FIG. 3. Effective valence versus height above first substrate atomic plane for a hollow adsorption site (dashed line) and bridge adsorption site (solid line); sodium on sodium (100). This calculation utilized the third of the given sets of scattering phase shifts.

2. Self-electromigration on low-Miller index Cu surfaces

In this section, we present the results of the application of the LKKR method to the case of adatom self-electromigration on Cu(100), Cu(110), and Cu(311). Figure 4 displays the calculated effective valence, normalized to the relaxation time (Z_w/τ), for the migration of a Cu adatom a Cu(100) substrate. The corresponding pathway for adatom migration on this substrate is illustrated in the accompanying schematic. Calculations were performed for an electric field applied in the orthogonal [010] and the [001] directions and, in each case, the components of the wind force were computed parallel and perpendicular to the field. As was the case for sodium self-electromigration, discussed in the previous section, the calculated off-diagonal elements of the valence tensor were approximately two orders of magnitude smaller than the diagonal elements. Consequently, Fig. 4 displays only the diagonal elements of Z_w/τ, plotted as a function of the lateral position of the adatom along a migration path that links a pair of fourfold hollow sites *via* the bridge site (see schematic).

Comparing Figs. 3 and 4, we see that the qualitative behavior of the wind force self-electromigration on Cu(100) is similar to that observed for Na migration on Na(100). In both systems, the valence tensor is almost diagonal and the diagonal elements are almost identical. This implies that the wind force is parallel to the electronic current and has a magnitude that is almost independent of the direction of **E**. Using the room-temperature bulk electronic relaxation time ($\tau \approx 1030$ a.u.), we estimate the effective valence for self-electromigration on Cu(100), averaged between the hollow and bridge sites, to be $\langle Z_w \rangle = -28.1$. This value is somewhat larger than the value of $\langle Z_w \rangle = -21.4$ computed for self-electromigration on Cu(111).[15] Given the apparent ballistic nature of the wind force for Cu migration on Cu(100) and Cu(111), this difference then reflects the difference in the

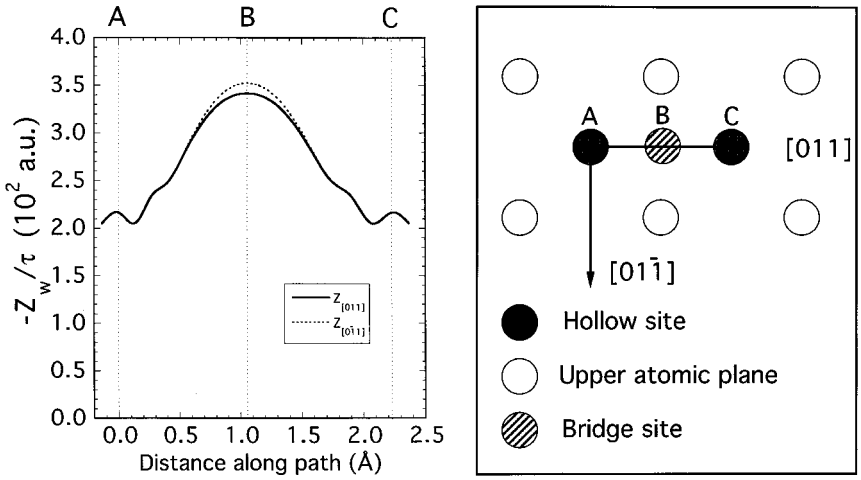

FIG. 4. Component of the effective valence versus distance moved along given migration path on copper (100). $Z_{[011]}$ and $Z_{[0\bar{1}1]}$ are the valence tensor elements corresponding to wind forces in the [011] and [01$\bar{1}$] directions for applied electric fields in the same ([011] and [011], respectively) directions. The schematic shows the investigated migration pathway.

local density of conduction-electron states in the vicinity of a Cu adatom on Cu(100) and Cu(111). Since an adatom on Cu(100) is more highly coordinated than an adatom on Cu(111), one anticipates that $n(\mathbf{r})$ and, consequently, Z_w will be greater for Cu(100) than for Cu(111).

When the adatom is located above the hollow site of Cu(100), the fourfold symmetry of the substrate implies that the wind force is identical when the field is applied in (equivalent) [010] and the [001] directions. For other positions along the migration pathway, the forces for these two field directions are expected to be inequivalent. Consequently, we observe a slight ($\approx$3%) difference in the magnitude of the two diagonal elements of Z_w/τ, which is maximal at the bridge site. The variation represents the influence of the local scattering geometry of the adatom, which changes as the adatom is moved along the migration path.

In Fig. 5, we show the calculated wind force for self-electromigration on Cu(100), plotted as a function of the adatom adsorption height. Results are shown for the adatom located above the fourfold hollow and twofold bridge sites. In contrast to the case of Na electromigration on Na(100), for a range of Cu adatom adsorption heights ($3.4 \geqslant h \geqslant 1.2$ Å), we observe a substantial difference in the magnitude of the wind force calculated for the distinct sites. While the force is ballistic in origin, the local density of conduction-electron states outside of Cu(100) is not well described by the free-electron model. Specifically, $n(\mathbf{r})$ for Cu(100) is more strongly site-dependent than for Na(100).

Figure 6 shows the calculated effective valence for the migration of a Cu adatom on Cu(110). In this case, we display the diagonal elements of Z_w/τ calculated for the electric field applied parallel the [110] and [001] directions. As for Cu(100), the calculated valence tensor is almost diagonal and the diagonal elements are negative. The difference between the diagonal elements of Z_w/τ varies by $\approx$2% when the adatom is located at the hollow site and $\approx$10% at the long bridge site. We note that the wind force is almost parallel to the field and has a magnitude that is almost independent of the field direction, even though the Cu(110) substrate unit cell is rectangular, so that the directions in which the field is applied are inequivalent. The calculated effective valence, averaged between the hollow and bridge sites, is found to be $Z_w = -2.9.1$ for the applied field and migration path parallel to the [110] direction.

Figure 7 displays the calculated effective valence for self-electromigration on Cu(311). We considered a migration pathway that links together two continuation hollow sites, labeled *A* and *C*, *via* another, inequivalent, hollow site *C* (see schematic). The Cu(311) substrate is a slightly stepped surface on which the steps are parallel to the [011] direction. The migration pathway crosses a step edge on the segment linking points *B* and *C* shown in Fig. 7. Therefore, this system allowed the investigation of the influence of simple step structures upon the electromigration wind force.

Effective valences were computed for electric fields applied parallel and perpendicular to the step edge that lies parallel [011] direction. For all position on the migration pathway, the valence tensor was diagonal dominant; the off-diagonal elements were approximately two orders of magnitude smaller than the diagonal elements. The averaged diagonal elements of the valence tensor for distinct segments of the migration pathway are presented in Table I.

Our results demonstrate a significant asymmetry in the wind force as the Cu adatom traverses the step edge on a Cu(311) substrate. First, we note that there exists a marked asymmetry in the calculated valence tensor under the simultaneous reversal of the migration path and the applied field. Specifically, consider the path that crosses the step edge to

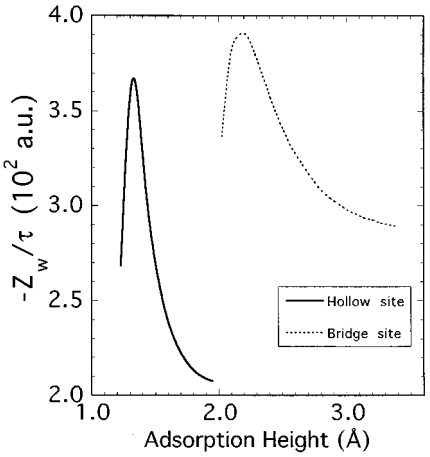

FIG. 5. Effective valence versus height above the first substrate atomic plane for a hollow adsorption site (solid line) and bridge adsorption site (dashed line); copper on copper (100).

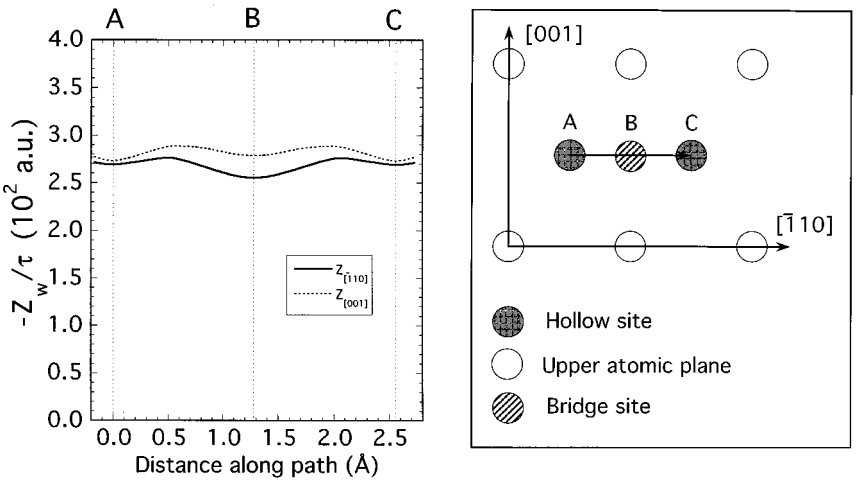

FIG. 6. Component of the effective valence versus distance moved along given migration path on copper (110). $Z_{[001]}$ and $Z_{[1\bar{1}0]}$ are the valence tensor elements corresponding to wind forces in the [001] and [1̄10] directions for applied electric fields in the same ([001] and [110], respectively) directions. The schematic shows the investigated migration pathway.

link the sites labeled *B* and *C* (see Fig. 7). If the electric field is applied parallel to the step from $B \rightarrow C$ ([233]), the calculated wind force experienced by the adatom is antiparallel to **E** and favors migration from $C \rightarrow B$. The valence, averaged along the path $C \rightarrow B$ is found to be $\langle Z_w \rangle - 22.9$, see Table I. When the field is applied in the opposite direction, $C \rightarrow B$, migration occurs along $B \rightarrow C$ with a average valence of $\langle Z_w \rangle - 27.7$. Thus, we observe a significant difference in the magnitude of the electromigration wind force, experienced by adatoms that cross a step edge, when the field is applied in the ''up-'' or ''down-step'' directions.

We also observe that the magnitude of the average wind force for migration between two sites on the same terrace, *A* and *B*, is always greater than that experienced by an adatom along a path that the crosses a step edge, *B* to *C*. This reflects the fact that diffusion between the sites *B* and *C* involves transfer across the low coordination step edge, where the adatom experiences in a region of reduced conduction-electron density, compared to motion along a terrace.

Finally, it is informative to compare the results of the LKKR calculation applied to copper self-electromigration results to the quantitative predictions of the ballistic model of the wind force.[16,43] According to this simple model, the wind force acting upon an adatom is parallel to the electronic current and is proportional to the transport cross section of the adatom $\sigma_{\rm tr}(E_F)$,[44] the local density of conduction electrons, $n(\mathbf{r})$, and the mean free path *l*:

$$\mathbf{F}_w = \mathbf{E} e Z_w = \mathbf{E} e (-n_0 l \sigma_{\rm tr}). \tag{45}$$

For electromigration in bulk Cu, $n = 8.45 \times 10^{-2}$ Å^{-3},[18] $l = 393$ Å at 293 K (Ref. 18) and the transport cross section, computed from the Cu phase shifts employed in our layer-KKR calculation and found to be $\sigma_{\rm tr} = 1.29$ Å^2 at the Cu Fermi energy. It follows that the ballistic estimate for the effective valence in bulk Cu is $Z_w = -43.2$. Therefore, for all of the Cu surfaces and migration pathways considered, we find that the calculated effective valence for the surface electromigration of Cu adatoms is significantly smaller than that for bulk self-electromigration. Given the qualitatively ballistic nature of the calculated forces, this difference may be attributed to the reduction of conduction-electron density, $n(\mathbf{r})$ at a Cu surface, relative to that of the bulk. Further, we find that there is a direct correlation between the coordina-

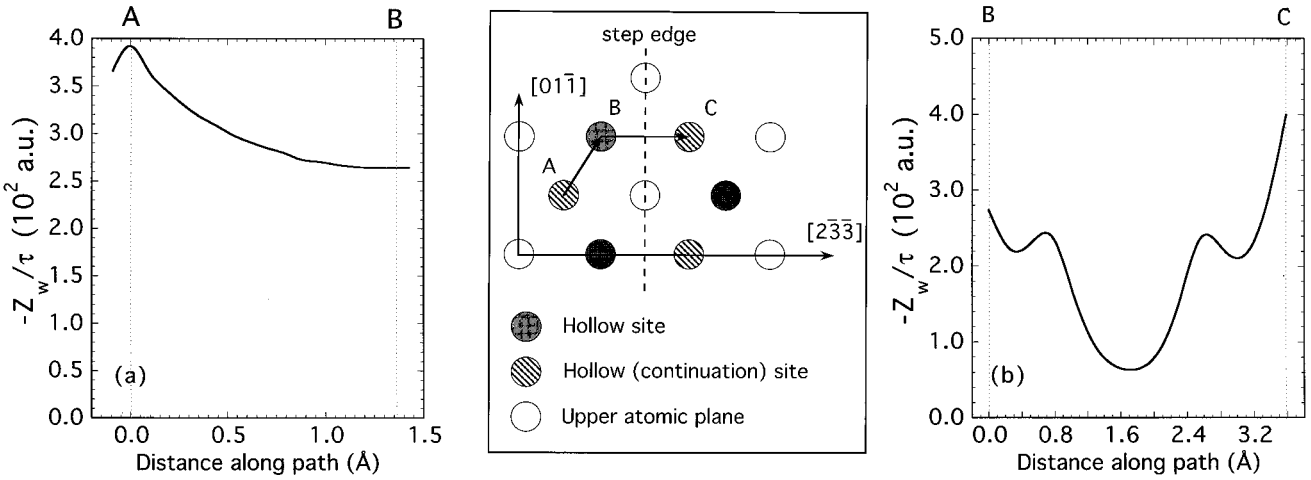

FIG. 7. Components of the effective valence versus distance moved along given migration paths on copper (311). The schematic shows the investigated migration pathway. (a) The pathway from point *A* to point *B* (see schematic). (b) The pathway from point *B* to point *C*. In each case, we consider the diagonal valence element coupling an applied field along the migration direction to the wind force in the same direction.

TABLE I. Effective wind valences calculated for the different path segments shown in Fig. 7. In each case, the applied field is parallel to the path.

Diffusion step	Effective valence
$A \rightarrow B$	−33.5
$B \rightarrow A$	−29.4
$B \rightarrow C$	−22.9
$C \rightarrow B$	−27.7

tion of an adatom and the magnitude of the average wind valence for similar migration pathways. Specifically, the magnitude of the wind force increases as the substrate becomes more open.

3. Impurity electromigration at Cu surfaces

In this section, we describe the results of the LKKR calculation applied to the computation of the wind force acting upon impurity adatoms on Cu substrates. Figures 8(a), 8(b), and 8(c) display the normalized wind valence for the electromigration of Al, Na, Si, and W adatoms on Cu(100), Cu(110), and Cu(311), respectively. The figure shows diagonal element of the valence tensor corresponding to the wind force acting in the same direction as an field applied in the [011] direction. For every adatom considered, the off-diagonal elements of the effective valence tensor were smaller than the diagonal elements by at least two orders of magnitude. The qualitative behavior of the wind force, as a function of the adatom lateral position, is similar for each of the adatoms and substrates, displaying a small variation between distinct adsorption sites.

According to the ballistic model of the electromigration, the magnitude of the wind valence is proportional to the transport cross section of the migrator and the density of conduction electron states in the vicinity of the adatom. In order to explore the correlation between Z_w and σ_{tr}, we display in Fig. 9 the calculated average wind valence for Al, Na, Si, W, and Cu electromigration on Cu(110), Cu(100), and Cu(311), plotted as a function of the transport cross section of each migrator. The transport cross sections, computed using the phase shifts used in our LKKR calculations, were for Na, $\sigma_{\mathrm{tr}}=0.014$ Å^2; for Cu, $\sigma_{\mathrm{tr}}=1.30$ Å^2; for Al, $\sigma_{\mathrm{tr}}=1.91$ Å^2; for Si, $\sigma_{\mathrm{tr}}=2.91$ Å^2; and for W, $\sigma_{\mathrm{tr}}=5.85$ Å^2.

From Fig. 9 we observe that, to a good approximation, the average wind valence is proportional to the transport cross section of the adatom, in agreement with the predictions of the simple ballistic model. The slope of the line, equal in the ballistic model to nl/τ, is found to have its highest value for the (311) surface and lowest value for the (100) surface. Therefore, the results presented in Fig. 9 are suggestive of the reduction of electron density, along the surface migration paths, for closer packed surfaces.

VII. CONCLUSIONS

We have presented a quantitative investigation of the electromigration wind force at metallic surfaces, using a layer-KKR method to evaluate the electron-scattering states. For self-electromigration and impurity electromigration on Cu and Na substrates, our results suggest that the wind force

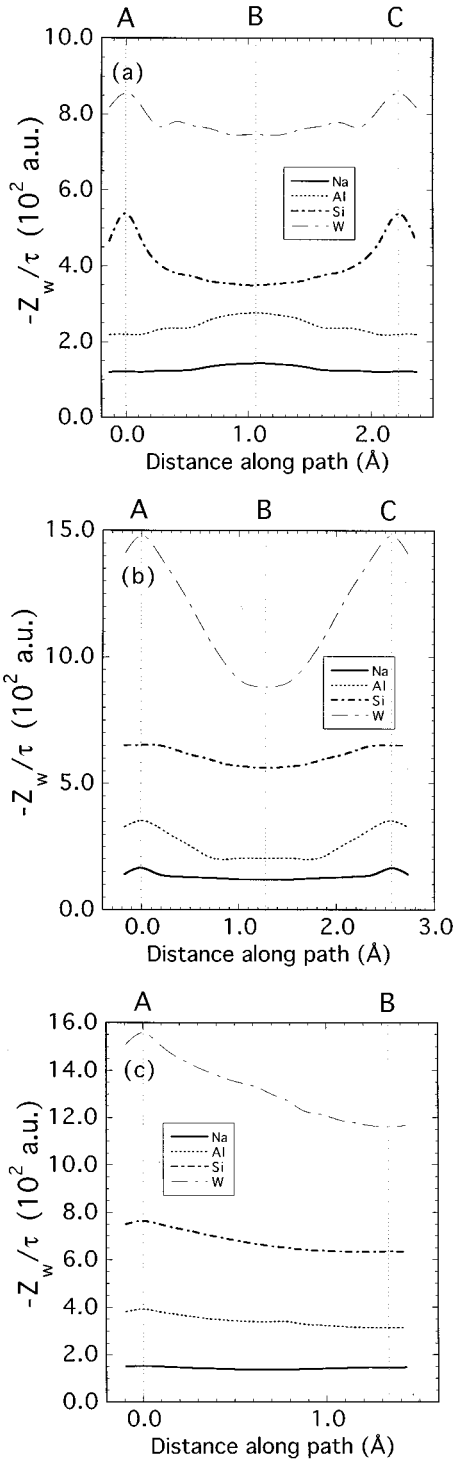

FIG. 8. Components of the effective valence versus distance moved along the migration pathway for inhomogeneous electromigration on copper (100) (a), copper (110) (b), and copper (311) (c). Results are given for sodium (solid line), aluminum (dotted line), silicon (short dash-dotted line), and tungsten (long dash-dotted line). For each surface orientation, we give one (diagonal) element of the valence tensor for each species in order to illustrate the differences in behavior between them. For the (100) surface: applied field and force in the [011] direction. For the (110) surface: applied field and force in [$1\underline{1}0$] the direction. For the (311): applied field and force in the [011] direction.

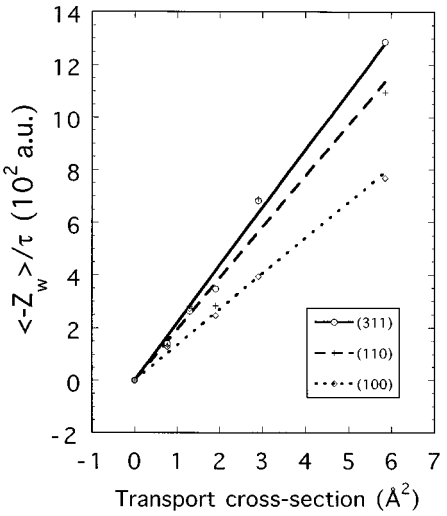

FIG. 9. Average wind force between adsorption sites versus transport cross section for inhomogeneous electromigration on low index copper surfaces. Lines are least-squares fits for each of the three surface orientations; solid for copper (311), short dashes for copper (110), dots for copper (100).

experienced by an isolated adatom is quite well described by a simple ballistic model if the reduction of the electron density at the surface, relative to the bulk, is taken into account. The conclusion is supported by the strong dependence of the magnitude of the calculated wind force upon the adatom height, a result which suggests a correlation of the wind force with the decreasing electronic density of states outside of the substrate.

The apparent success of the free-electron ballistic model in predicting the qualitative features of surface electromigration on Cu substrates is perhaps surprising given that the layer-KKR calculation includes a quantitative model of the full electronic band structure. In addition, it is well known that the ballistic model fails to provide a quantitative description of the wind force for bulk electromigration in transition and noble metals, since it is applicable only within free-electron model.[43] Nevertheless, the agreement between the ballistic model and the layer KKR calculation, and, in particular, the isotropy of the computed wind force, suggests that the low coordination of an adatom relative to a substitutional impurity in the bulk plays a significant role in reducing the contribution to the wind force from multiple electron scattering in the vicinity of the adatom. The generality of this result will be explored in calculations of self-electromigration and impurity electromigration on Ag substrates, to be reported in a subsequent publication.

ACKNOWLEDGMENTS

The authors are pleased to acknowledge Dr. T. L. Einstein and Dr. Ellen D. Williams for helpful communications regarding this work. P.J.R. acknowledges the Donors of The Petroleum Research Fund, administered by the American Chemical Society, for partial support of this research. We also thank the National Science Foundation for partial support under Grant No. DMR 92-25080.

[1] For a useful review of Electromigration in metals, see Paul S. Ho and Thomas Kwok, Rep. Prog. Phys. **52**, 301 (1989).
[2] A. H. Verbruggen, IBM J. Res. Dev. **32**, 93 (1988).
[3] C. Bosvieux and J. Friedel, J. Phys. Chem. Solids **23**, 123 (1963).
[4] Rolf Landauer and James F. Woo, Phys. Rev. B **10**, 1266 (1974).
[5] R. S. Sorbello, J. Phys. Chem. Solids **34**, 937 (1973).
[6] L. J. Sham, Phys. Rev. B **12**, 3142 (1975).
[7] W. L. Schaich, Phys. Rev. B **13**, 3350 (1976).
[8] H. Yasunaga and A. Natori, Surf. Sci. Rep. **15**, 205 (1992).
[9] I. V. Zakurdaev, G. I. Liberova, and V. N. Yakovlev, Fiz. Tverd. Tela (Leningrad) **21**, 456 (1979) [Sov. Phys. Solid State **21**, 270 (1979)].
[10] Yu. S. Vedula, Ukr. Fiz. Zh. (Russ. Ed) **14**, 132 (1969).
[11] Yu. S. Kaganovsk1, Ukr. Fiz. Zh. (Russ. Ed) **27**, 1070 (1982).
[12] P. Kumar and R. S. Sorbello, Thin Solid Films **25**, 25 (1975).
[13] T. W. Duryea and H. B. Huntington, Surf. Sci. **199**, 261 (1988).
[14] H. Ishida, Phys. Rev. B **49**, 14 610 (1994).
[15] T. L. Einstein, P. J. Rous, and E. D. Williams, Surf. Sci. Lett. **315**, 995 (1994).
[16] V. B. Fiks, Sov. Phys. Solid State **1**, 14 (1959).
[17] H. B. Huntington and A. R. Grone, J. Phys. Chem. Solids **20**, 76 (1961).
[18] Neil W. Ashcroft and N. David Mermin, *Solid State Physics* (Saunders College, Philadelphia, 1987).
[19] R. S. Sorbello, Phys. Rev. B **39**, 5119 (1981).
[20] J. van Ek and A. Lodder, J. Phys. Condens. Matter **3**, 7307 (1991); **3**, 733 (1991); **3**, 8403 (1991).
[21] Raju P. Gupta, Phys. Rev. B **25**, 5188 (1982).
[22] R. S. Sorbello, Phys. Rev. B **39**, 4984 (1989).
[23] C. S. Chu and R. S. Sorbello, Phys. Rev. B **38**, 7260 (1988).
[24] G. Brebec, R. P. Gupta, Y. Serruys, and Y. Adda, Phys. Rev. B **27**, 672 (1983).
[25] A. Lodder, Physica A **158**, 723 (1989).
[26] We utilize atomic units with $m_e=\hbar=1$.
[27] Ryogo Kubo, J. Phys. Soc. Jpn. **12**, 570 (1957).
[28] G. D. Gaspari and B. L. Gyorffy, Phys. Rev. Lett. **28**, 801 (1972).
[29] W. H. Butler, in *Physics of Transition Metals, 1980*, edited by P. Rhodes, IOP Conf. Proc. No. 55 (Institute of Physics and Physical Society, London, 1981), p. 505.
[30] J. B. Pendry, *Low Energy Electron Diffraction* (Academic, New York, 1974).
[31] W. H. Weinberg, M. A. Van Hove, and C. M. Chan, *Low-Energy Electron Diffraction* (Springer-Verlag, Berlin, 1986).
[32] M. A. Van Hove and S. Y. Tong, *Surface Crystallography by LEED* (Springer-Verlag, Berlin, 1979).
[33] K. Kambe, Z. Naturforsch. Teil A **22**, 442 (1967).
[34] K. Kambe, Z. Naturforsch. Teil A **22**, 322 (1967).
[35] K. Kambe, Z. Naturforsch. Teil A **23**, 1280 (1968).
[36] D. D. Vvedensky, J. M. Maclaren, S. Crampin, and J. B. Pendry, Phys. Rev. B **40**, 12 164 (1989).
[37] P. J. Jennings, R. O. Jones, and O. Jepsen, Phys. Rev. B **29**, 6474 (1984).
[38] C. T. Chen, N. V. Smith, and M. Weinert, Phys. Rev. B **40**, 7565 (1989).

[39] S. L. Cunningham, Phys. Rev. B **10**, 4988 (1974).

[40] The l-resolved phase shifts employed by Duryea and Huntington in their seminal work on sodium electromigration and used by us here are: {0.298, 0.276, 0.061, 0.010}, {0.414, 0.3160.062, 0.009}, {0.373, 0.321, 0.042, 0.001}, given in the form $\{\delta_{l=0}, \delta_{l=1}, \delta_{l=2}, \delta_{l=3}\}$.

[41] For example, the *minimum* values of the diagonal to off-diagonal valence tensor elements for an applied field in the [010] direction were: 48.2, 38.3, and 34.9 for the first, second, and third sets of phase shifts, respectively.

[42] William B. Pratt, Jr., Peter A. Schroeder, and Jack Bass, Rev. Mod. Phys. **62**, 645 (1990).

[43] R. S. Sorbello, in *Materials Reliability Issues in Microelectronics*, edited by J. R. Lloyd, P. S. Ho, C. T. Sah, and F. Yost, MRS Symposia Proceedings No. 225 (Materials Research Society, Pittsburgh, 1991), p. 3.

[44] R. S. Sorbello and C. S. Chu, IBM J. Res. Dev. **32**, 1 (1988).